

1 Highlights

2 **The role of ocean circulation in driving hemispheric symmetry breaking of the ice shell of** 3 **Enceladus**

4 Wanying Kang, Suyash Bire, John Marshall

- 5 • Ocean circulation can transport heat across the equator enhancing the hemispheric asymmetry in ice shell thick-
6 ness.
- 7 • The asymmetry can be enhanced (suppressed) by ocean circulation if heating occurs mostly in the ice shell
8 (silicate core).
- 9 • The coupled ocean-ice system may have multiple equilibria.

The role of ocean circulation in driving hemispheric symmetry breaking of the ice shell of Enceladus

Wanying Kang^a, Suyash Bire^a and John Marshall^a

^aEarth, Atmospheric, and Planetary Sciences, Massachusetts Institute of Technology, Cambridge, MA 02139 US

ARTICLE INFO

Keywords:

Icy moon

ocean circulation

Enceladus

ABSTRACT


The ice shell of Enceladus exhibits strong asymmetry between its hemispheres, with all known geysers concentrated over the south pole, even though its orbital configuration is almost perfectly symmetric. By exploring ocean circulation across a range of ocean salinities and core/shell heating partitions, we study the role of ice-ocean interaction in hemispheric symmetry breaking. We find that: (i) asymmetry is enhanced by cross-equatorial ocean heat transport when the ice shell is the major heat source and vice versa, (ii) the magnitude of ocean heat transport is comparable to the global heat production, significantly affecting the ice shell evolution and equilibrium state and (iii) more than one equilibrium state can exist due to a positive feedback between melting and ocean circulation.

1. Introduction

Beneath the ice shell encasing Enceladus, a small icy moon of Saturn, a global ocean of liquid water (Postberg et al., 2009; Thomas et al., 2016) ejects geyser-like sprays into space through fissures concentrated near the south pole (Hansen et al., 2006; Howett et al., 2011; Spencer and Nimmo, 2013; Waite et al., 2017), making it one of the places with the highest potential of finding extra-terrestrial life. However, it remains a puzzle as to why all geysers concentrate near the south pole (Howett et al., 2011; Iess et al., 2014; Porco et al., 2007). Enceladus is tidally locked to Saturn with almost zero obliquity, and so tidal heating patterns will be almost perfectly symmetric between the two hemispheres in the absence of an asymmetry in the ice shell (Chen, E M A and Nimmo, F, 2011; Baland et al., 2016).

It has been suggested that hemispheric asymmetry could stem from an a-priori anomaly due to a giant impact and/or a monopole structure in geological activity (Han and Showman, 2010; Behoukova et al., 2012; Rozel, A et al., 2014; Roberts and Stickle, 2021). It is supposed that on geological timescales, this anomaly then moves over the south pole by true polar wandering (Nimmo and Pappalardo, 2006; Stegman et al., 2009; Tajeddine et al., 2017). However, given that currently there is only one such hot spot on Enceladus, implicit assumptions have to be made about the frequency of giant impacts and their recovery time.

Hemingway et al. (2019) propose that the ice shell could be torn apart by the overpressure induced by a freezing of the subsurface ocean. Since the ice shell is thinnest and hence weakest over the poles, due to the polar-amplified tidal

 wanying@mit.edu (W. Kang); bire@mit.edu (.S. Bire); jmarsh@mit.edu (J. Marshall)
ORCID(s):

44 dissipation in the ice shell and core (Beuthe, 2013; Choblet et al., 2017), the initial fracture would most likely occur at
45 one of the poles. Once this happens, the pressure would be released thus preventing a similar event from happening
46 over the other pole. The enhanced dissipation from polar venting will further thin the ice there.

47 Kang and Flierl (2020), instead, suggest that any small random asymmetry in ice shell thickness, be it induced
48 by giant impacts (Roberts and Stickle, 2021), obliquity tides (Tyler, 2009)) or other mechanisms, can amplify on
49 million-year timescales. The fastest growth occurs for thickness variations which have the gravest inter-hemispheric
50 scale, significantly thinning the ice shell at one of the poles and thereby promoting fracture formation there. The
51 hemispherically-asymmetric mode will grow and dominate over time for two reasons. First, rheology feedback makes
52 thin regions of the ice shell weaker and more mobile which in turn generates more heat and yet more thinning (Beuthe,
53 2019) — this enhances all thickness variations uniformly. Second, ice flow is more efficient at smoothing out thickness
54 variations which have small spatial scales than those with large scales (Ashkenazy et al., 2018). The combined action
55 of these two processes can account, it is argued, for both the concentration of geysers over one pole and the significant
56 hemispheric asymmetry in ice shell thickness.

57 Whatever the processes that influence the evolution of the ice shell, its freezing and melting will induce salinity
58 changes just under the ice, and its thickness variations will strongly influence the temperature at the water-ice interface
59 through the suppression of the freezing point of water with pressure — see Fig. 1a. Thus one can expect lateral salinity
60 and temperature gradients at the water-ice interface, both of which will drive ocean circulation. This circulation will
61 in turn redistribute heat (Tyler, 2014), reshaping the ice shell by inducing freezing and melting (Kang et al., 2021).
62 This interaction between the ice shell and the ocean just below it could provide an additional feedback, promoting,
63 or otherwise, hemispheric symmetry breaking. The focus of the present work is to study the possible role of cross-
64 equatorial ocean heat transport in enhancing or diminishing inter-hemispheric asymmetries in ice thickness.

65 **2. Explorations of cross-equatorial heat transport in a model of Enceladus' ocean** 66 **circulation**

67 We simulate the ocean circulation and its interaction with a poleward-thinning ice shell on an Enceladus-like icy
68 satellite, introduce small inter-hemispheric asymmetries in ice thickness and explore the efficacy of cross-equatorial
69 heat transport. The Massachusetts Institute of Technology ocean model (MITgcm, MITgcm-group, 2010; Marshall
70 et al., 1997) is employed in a zonally-averaged setup similar to, but slightly different from, that described in (Kang et al.,
71 2021). Instead of trying to understand the possible ocean circulation on Enceladus driven by the observed ice thickness
72 variations, here we use the method of perturbations to study the feedbacks at play when the ice shell is assumed to be
73 slightly asymmetric about the equator. Observations suggest a rather marked hemispheric asymmetry in ice thickness
74 (Iess et al., 2014; Beuthe et al., 2016; Tajeddine et al., 2017; Čadež et al., 2019; Hemingway and Mittal, 2019) but our

75 goal here is to investigate the ocean feedbacks — is a small asymmetry amplified or damped by ocean circulation and
 76 its associated ice-ocean interaction? Rather than the freezing/melting rate being prescribed, as in (Kang et al., 2021),
 77 here it depends on the circulation, allowing us to study feedbacks. Further details of the model configuration can be
 78 found in the supplementary materials (SM). Typically solutions take many thousands of years to reach equilibrium.

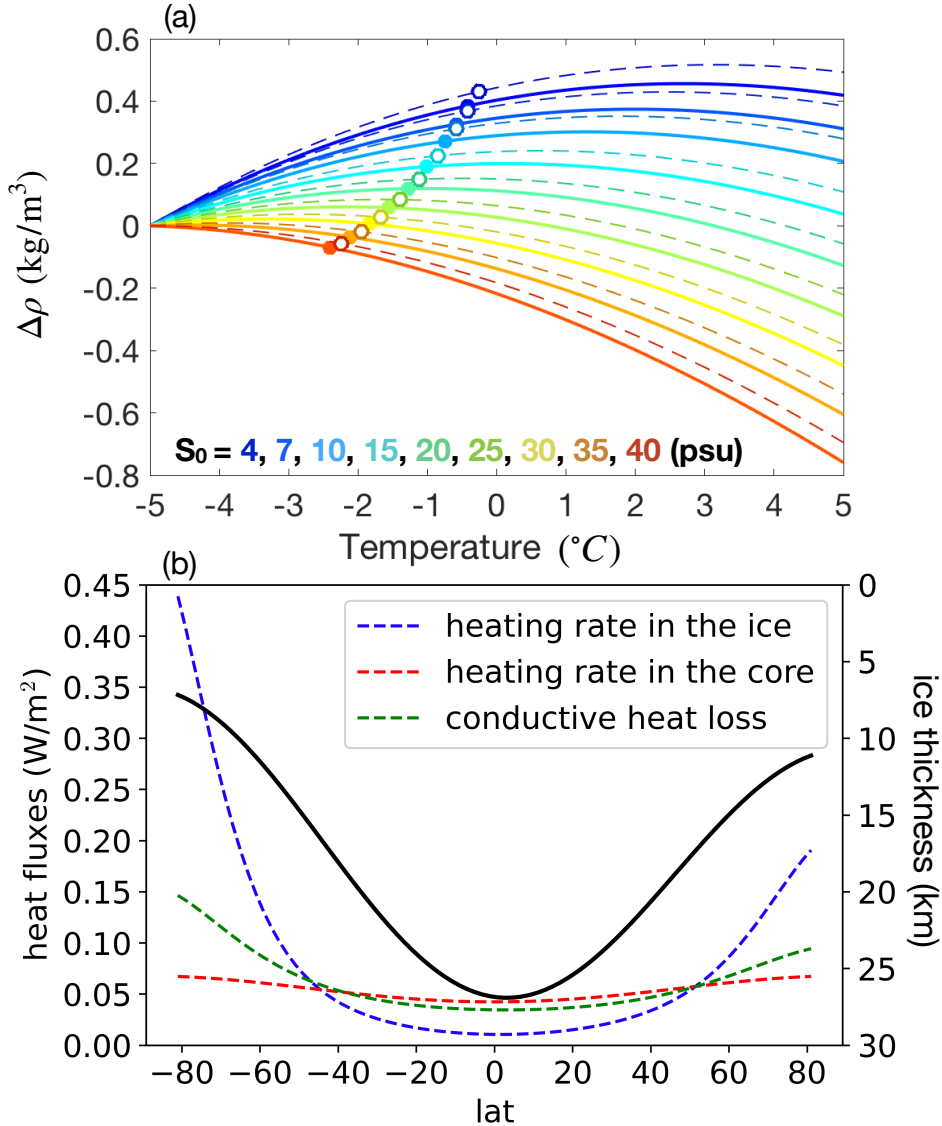


Figure 1: (a) The density anomaly of water near the freezing point as a function of temperature for various salinities and two different pressures. Cold to warm colors denote increasing salinity (see legend). The pressure beneath the 26-km thick ice shell at the equator is used to compute the solid curves and the pressure beneath the 7-km south polar ice shell is used for the dashed curves. In each case the density at -5 °C is chosen as a reference. The circles indicate the freezing point, full circles at the base of the equatorial ice shell and open circles at the base of the south polar ice shell: note the rightward shift of the open circles, which indicate the freezing point increases moving from equator to pole. (b) The ice shell thickness assumed here (solid curve, axis on the rhs) plotted as a function of latitude, along with the corresponding profiles of tidal heating in the ice shell (blue dashed, axis on the lhs), in the core (red dashed) and heat loss by conduction through the ice shell (green dashed). The global-mean of tidal heating in the core and the ice shell are set equal to the global-mean conductive heat loss.

79 The assumed ice thickness profile, which thins toward the poles and is slightly asymmetric about the equator —
 80 thinner over the south pole than the north — is shown by the black solid line in Fig.1b. The suppression of the
 81 freezing point on increasing pressure leads to temperature variations beneath the ice which induces a circulation. This
 82 redistributes heat, and exchanges with the ice modulate the freezing/melting (as set out in detail in Eqs. 13, 14, SM).
 83 This in turn changes the salinity through brine rejection/freshwater production (Eq. 16, SM). In our model, however, the
 84 ice shell geometry is not allowed to evolve under the assumption that lateral ice flow maintains balance ¹. Meanwhile,
 85 the core may also be a source of heat due to its tidal flexing, and is transmitted to the ocean through a bottom heat flux.
 86 Such core heating has been argued to be necessary to keep Enceladus from freezing up, given that the ice dissipation
 87 is likely insufficient at the present-day eccentricity (Beuthe, 2019; Choblet et al., 2017). According to Sandstrom’s
 88 theorem (Wunsch, 2005, Malte Jansen, private communication), both temperature and salinity forcings from the ice
 89 and the core can drive ocean circulation if buoyancy sinks occur higher up the water column than buoyancy sources.
 90 Furthermore, vertical diffusion may provide additional energy to the system by pumping dense water upward (Young,
 91 2010).

92 The normalized heat fluxes due to tidal dissipation in the shell and the core, together with the conductive heat loss
 93 through the ice shell, are shown in Fig. 1b. There the global-mean of the heat fluxes in the core and the ice shell are
 94 set equal to the global-mean conductive heat loss. In our experiments, the core/ice shell heat fluxes are also adjusted
 95 to guarantee that they exactly balance the globally-averaged conductive heat loss. Since regions with a thinner ice
 96 shell tend to be more dissipative (due to the ice rheology feedback) (Beuthe, 2019), heat production in the ice shell
 97 is concentrated over poles, and especially the south pole. Heating in the core, by contrast, is not affected by the ice
 98 thickness and is therefore assumed to be symmetric between the two hemispheres, as shown in Fig. 1b.

99 Under hemispherically-asymmetric forcing, a cross-equatorial overturning circulation forms in the ocean. If heat
 100 is carried from the northern hemisphere to the southern hemisphere by ocean circulation, the hemispheric asymmetry
 101 of ice thickness is enhanced, and vice versa. Given the limited knowledge of Enceladus’ ocean salinity (Postberg et al.,
 102 2009; Zolotov, 2007; Zolotov and Postberg, 2014; Glein et al., 2018; Ingersoll and Nakajima, 2016; Hsu et al., 2015;
 103 Kang et al., 2021) and the partition of heat production between the ice shell and the silicate core (Choblet et al., 2017;
 104 Beuthe, 2019; Kang et al., 2020), a series of experiments were carried out covering a range of ocean salinities (5,
 105 10, 15, 20 and 25 psu) and core/shell heat partitions (0%/100%, 20%/80%, 40%/60%, 60%/40%, 80%/20%, 100%/0%).
 106 Hereafter, we use $S_x s_y$ to refer to the experiment with a x psu salinity and $y\%$ of heat generated in the shell, s . It should
 107 be noted that the ice shell heating rates used in scenarios in which it is the dominant heat source is perhaps 1 order
 108 of magnitude higher than the predictions of tidal dissipation models, given our current understanding of ice rheology
 109 (Beuthe, 2019). Although more advanced models of ice rheology can lead to more heat production (Gevorgyan et al.,

¹We expect the results to remain similar with ice shell evolution on, and during the period of integration, we don’t expect significant change of ice geometry due to the long adjusting timescale.

110 2020), thus far, the attempt to fully account for purported heat losses has not yet been successful — see Robuchon
 111 et al. (2010); Shoji et al. (2013); Běhouňková et al. (2013); McCarthy and Cooper (2016); Beuthe (2019); Soucek et al.
 112 (2019); Gevorgyan et al. (2020).

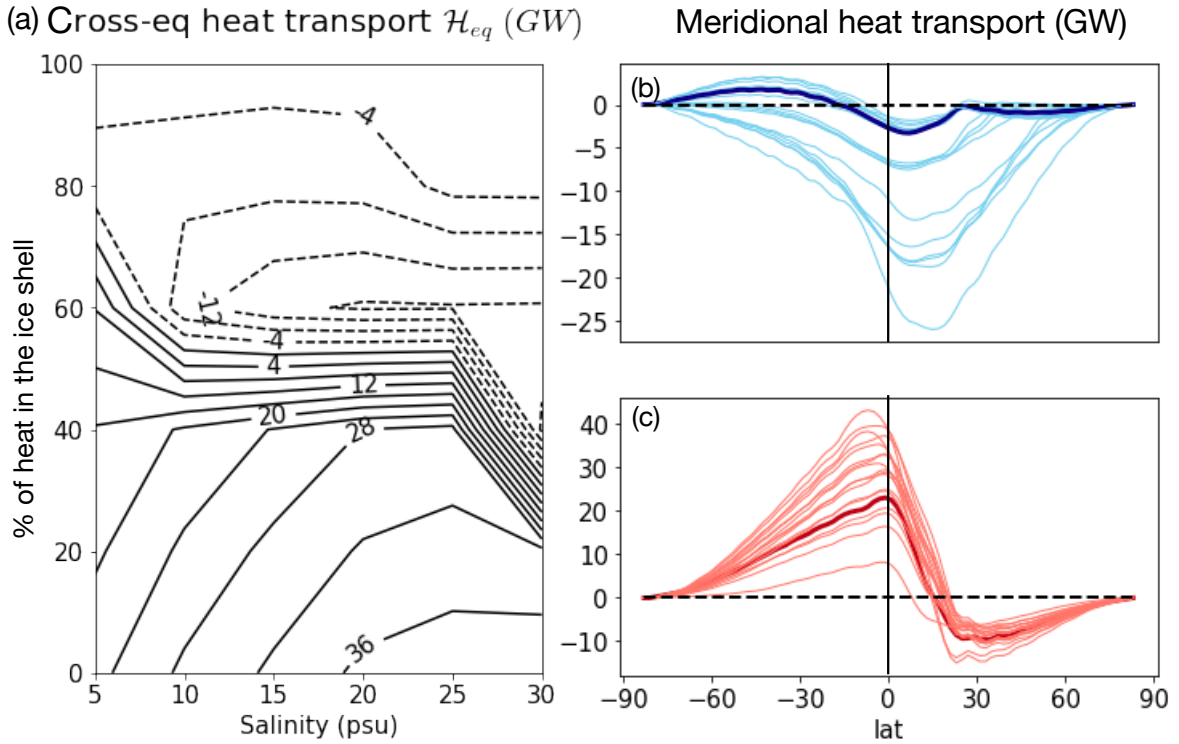


Figure 2: (a) Heat transport across the equator, H_{eq} , from a range of experiments assuming various heat partitions and ocean salinities: dashed lines are negative and continuous lines are positive. H_{eq} is southward/northward when heating dominates in the ice shell/core. Panel (b,c) show meridional heat transport profiles for experiments with southward (in red) and northward (in blue) cross-equatorial heat transport, respectively. Among all profiles, we use a thicker and darker curve to show the case with the highest salinity and shell heating (S30s80), and with the lowest salinity and shell heating (S5s0). These two solutions, representative of northward and southward cross-equatorial heat transport, are shown in more detail in Fig. 3.

113 A key finding of our study is summarized in Fig.2(a), where cross-equatorial heat transport is shown for various
 114 ocean salinities and core-shell heat partitions. We see that when most of the heating is assumed to be in the ice shell,
 115 ocean circulation tends to carry heat from the northern hemisphere to the southern hemisphere. This induces melting in
 116 the southern hemisphere where the ice shell is already thin, enhancing hemispheric asymmetry. The opposite happens
 117 when heating is assumed to dominate in the core. Ocean salinity plays a secondary role through its affect on the sign
 118 and magnitude of the thermal expansion coefficient, the slope of the curves shown in Fig.1a.

119 We use the direction of equatorial heat transport as a criterion to separate our experiments into two groups, one
 120 which enhances hemispheric asymmetry in the ice shell (negative/southward cross-equatorial heat transport) and the
 121 other that suppresses it (positive/northward cross-equatorial heat transport). Panel (b) and (c) in Fig.2 show the merid-

122 ional heat transport profiles for the these two groups, respectively. Conspicuously, the pattern of heat transport profiles
 123 are broadly the same within each group, attesting to the similarity of their ocean circulation and thermodynamic states
 124 (not shown). The solution with the highest salinity and shell heating (S30s80 — asymmetry-enhancing), and the lowest
 125 salinity and core heating (S5s0 — asymmetry-suppressing) are shown in more detail in Fig.3.

126 Both groups converge heat toward the equator, but the amplitude is much stronger in the asymmetry-suppressing
 127 group which have the preponderance of heating coming from the core. Since the global heat flux lost by the moon
 128 is around 35-40 GW (Beuthe, 2019), convergence of such large quantities of heat toward the equator, as is typical of
 129 asymmetry-suppressing scenarios, would ultimately lead to melting of the equatorial ice shell, rendering it impossible
 130 to sustain the observed equator-to-pole ice thickness gradient. A typical asymmetry-suppressing scenario has over 50%
 131 of the global heat flux (20-30 GW) transported to the northern hemisphere, where the ice is thicker, sufficient to suppress
 132 the development of asymmetry. Furthermore, the observed asymmetry of Enceladus' ice shell is much stronger than
 133 prescribed here (Iess et al., 2014; Beuthe et al., 2016; Tajeddine et al., 2017; Čadek et al., 2019; Hemingway and Mittal,
 134 2019), making the situation even more problematic for retention of the observed ice shell geometry.

135 In the remainder of our paper, we describe the contrasting circulations of the asymmetry-enhancing and asymmetry-
 136 suppressing solutions and then go on to discuss the mechanisms that facilitate cross-equatorial heat transport and hence
 137 symmetry-breaking.

138 **3. Contrasting ocean circulations driven by shell-dominated vs core-dominated heating**

139 In the ice shell-heating solutions, the highly polar-amplified heating profile (blue dashed curve in Fig.1b) induces
 140 melting over the poles (especially the south pole) and freezing elsewhere. This reduces the salinity over the polar
 141 regions compared to the equator (Fig.3-b1). Temperature is higher under the thin ice shell over the poles because the
 142 freezing point is higher when the ice shell is thinner. This is manifested by the rightward shift of the open circles
 143 (which indicate the freezing point at the base of the south polar ice shell) relative to the filled circles (marking the
 144 freezing point at the base of the equatorial ice shell) in Fig.1a. When salinity is higher than 22 psu (the case shown has
 145 a salinity of 30 psu), the thermal expansion coefficient of water (given by the slopes of the curves in Fig.1a) is positive.
 146 Thus both high temperature and low salinity make polar waters lighter than equatorial waters (Fig.3-c1). This induces
 147 downwelling in low latitudes and upwelling in high latitudes (Fig.3-d1). Through mixing of warm polar water with
 148 cold equatorial water, heat is converged toward the equator (Fig.2b).

149 If most heat is generated in the core, the heating profile is oblivious to the poleward-thinning ice shell geometry
 150 but, nevertheless, is slightly polar-amplified (red dashed curve in Fig.1b). Instead of being directly transmitted to the
 151 ice shell, this moderate polar amplification in heating is overwhelmed by the equatorward heat convergence (Fig.2c),
 152 leading to melting of ice at low latitudes and freezing at high latitudes. As a result, the salinity of equatorial (polar)

Ocean Circulation on Icy Moons

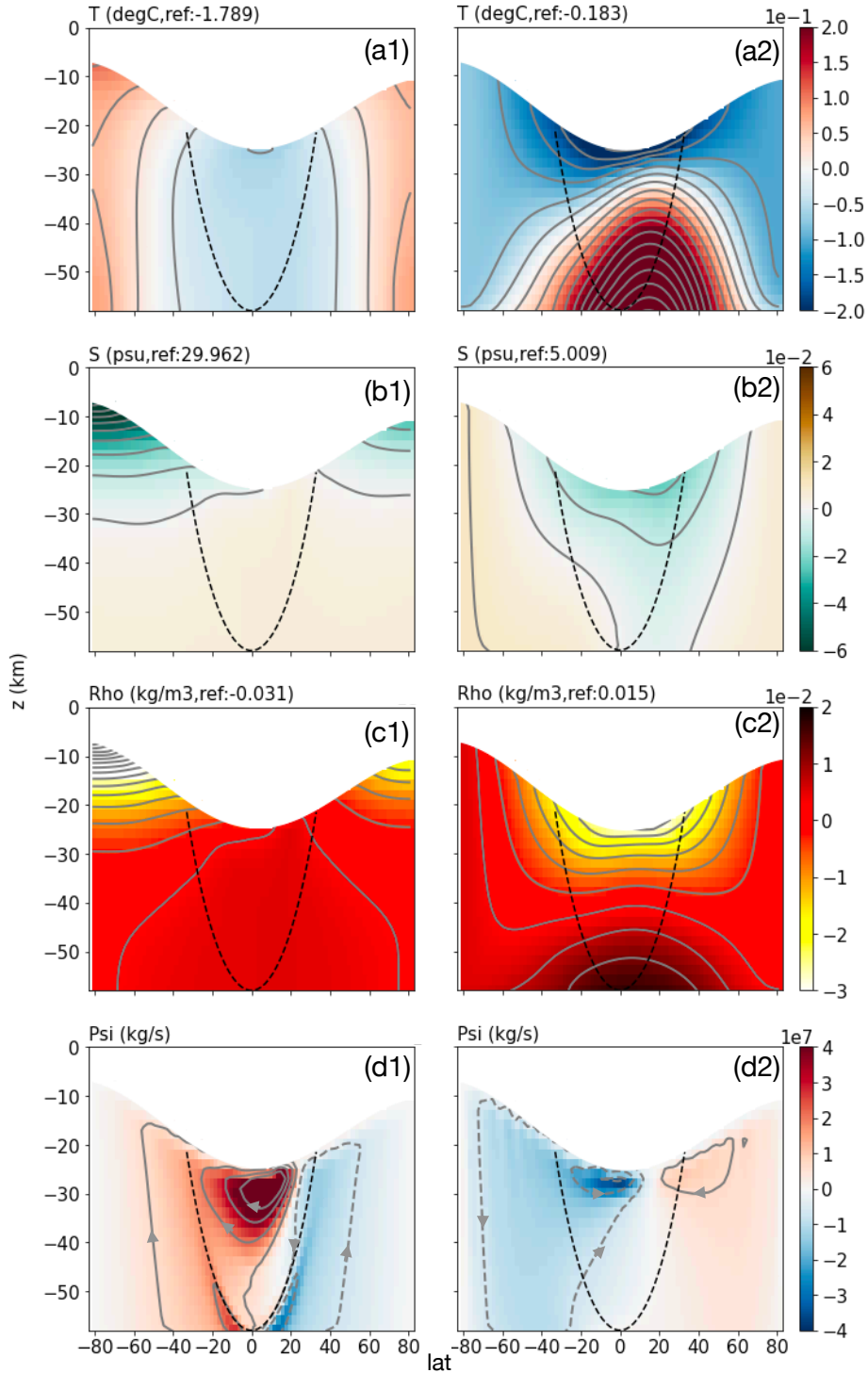


Figure 3: Typical circulation and thermodynamic ocean state of (column 1) the core-heating, asymmetry-enhancing group and (column 2) the shell-heating, asymmetry-suppressing group. The asymmetry-enhancing solution has the highest salinity and shell heating (S30s80), and the asymmetry-suppressing solution has the lowest salinity and core heating (S5s0). Moving from top to bottom we present temperature T , salinity S , density anomaly $\Delta\rho$ and the meridional overturning streamfunction Ψ with arrows to indicate the sense of circulation. The reference temperature and salinity (marked at the top of each plot) are subtracted from T and S enabling us to better capture the spatial patterns. Positive Ψ indicates a clockwise overturning circulation. The contour intervals are 0.04K, 0.01 psu, 0.005 kg/m³ and 1.2×10^7 kg/s from top to bottom. The tangent cylinder is shown by the dashed line in each panel.

153 waters is brought down (up), as can be seen in Fig.3-b2. Since the case shown has a salinity of 5 psu, lower than the
 154 22 psu transition point, water expands upon cooling (Fig.1a). Thus, in contrast to the shell-heating group, both high
 155 temperature (Fig.3-a2) and high salinity (Fig.3-b2) make polar waters denser rather than lighter than equatorial waters.
 156 This drives an ocean circulation in the opposite direction to the shell-heating case, with sinking in high latitudes and
 157 upwelling in low latitudes (Fig.3-d2). The equatorward flow in the deeper ocean picks up heating from the seafloor,
 158 should it be present, carrying heat toward the equator. This is in addition to equatorward heat transport associated with
 159 mixing between polar water and equatorial water. The net result is a much stronger convergence of heat to the equator
 160 in this asymmetry-suppressing group compared to the asymmetry-enhancing group (Fig.2c).

161 It should be noted that heat is converged toward low latitudes in all experiments, just as described in Kang et al.
 162 (2021). This indicates that the ice thickness gradient between equator and poles will always be reduced by ocean
 163 circulation (Fig.2b,c). If this cannot be counterbalanced by polar-amplified tidal heating in the ice, the equator-to-pole
 164 thickness gradient will erode over time, leading to a state which would be inconsistent with the observed ice geometry
 165 (Iess et al., 2014; Beuthe et al., 2016; Tajeddine et al., 2017; Āadek et al., 2019; Hemingway and Mittal, 2019).

166 Finally, we note that not only are the overturning circulations of the two solutions of opposite sign, but they are also
 167 slightly shifted relative to the equator, one north the other south. It is this shift that leads to cross-equatorial transport
 168 of heat and the possibility of symmetry-breaking in ice thickness, as we now discuss.

169 **4. Mechanisms behind cross-equatorial heat transport and symmetry breaking**

170 Ocean circulation can enhance or suppress symmetry breaking by transporting heat across the equator. This can
 171 be facilitated by a circulation that straddles the equator connecting the two hemispheres together, much as our earth's
 172 ocean's overturning circulation connects the northern and southern hemispheres, resulting in cross equatorial heat
 173 transport in the Atlantic sector — see, for example, the review by Buckley and Marshall (2016). On earth, the ocean's
 174 are confined in basins defined by coasts that cross the equator and support western boundary currents. These boundary
 175 currents facilitate cross equatorial transport, for example in the giant meridional overturning circulation of the Atlantic
 176 ocean. In our simulations of Enceladus, there are no such topographic assists to cross-equatorial transport because,
 177 in the absence of observational constraints, our model assumes a flat bottom. Instead, the top and bottom boundaries
 178 provide the necessary friction and ageostrophic flow to support an overturning circulation. Due to the hemispheric
 179 asymmetry in the forcing, the overturning cells move (slightly) away from the equator, leading to cross-equatorial
 180 heat transport. In the asymmetry-enhancing cases, water crosses the equator in the interior ocean and returns near the
 181 surface (Fig.3-d1). The opposite is true in the asymmetry-suppressing cases (Fig.3-d2). We now build a simple model
 182 of the cross-equatorial heat transport.

183 The cross-equatorial heat transport, \mathcal{H}_{eq} , is jointly controlled by the inter-hemispheric mass exchange, which can

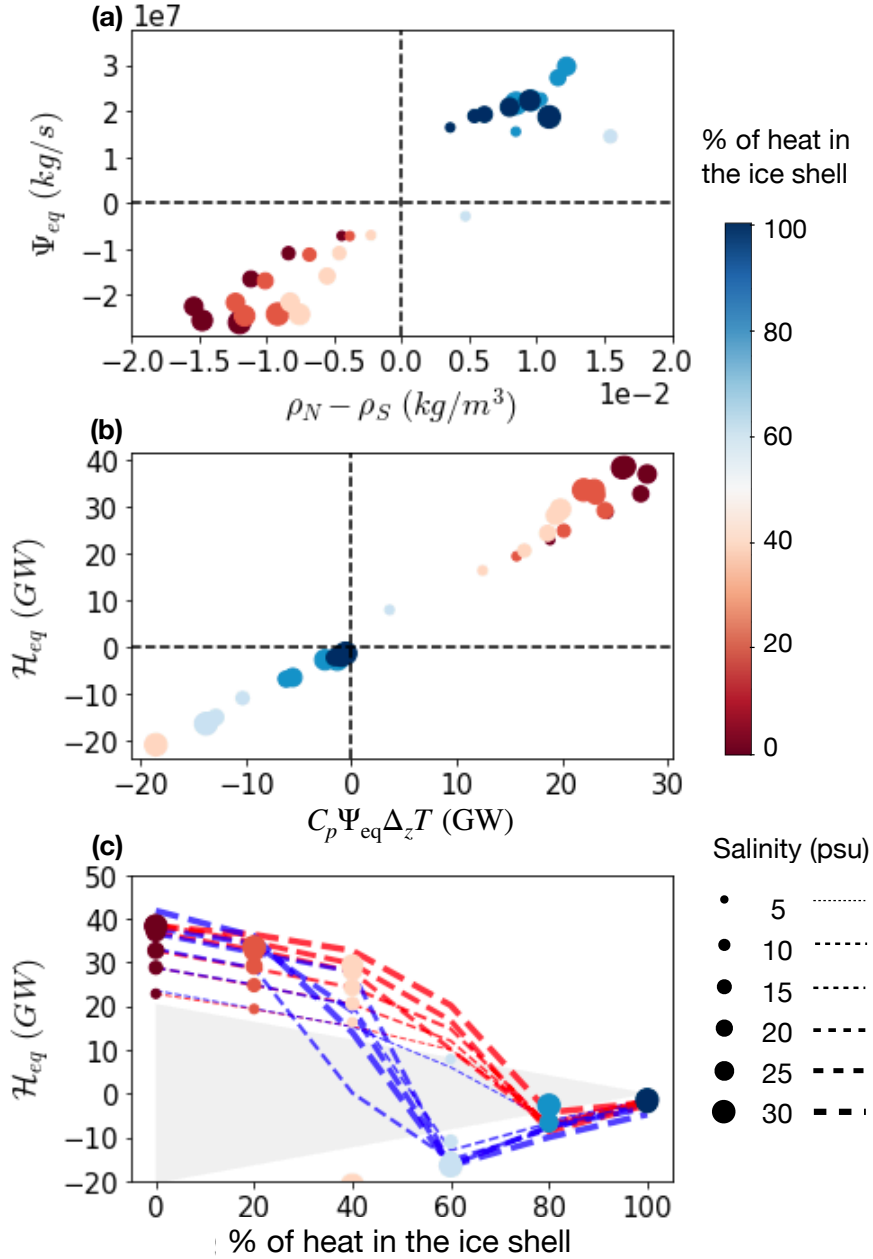


Figure 4: (a) The correlation between the cross-equator overturning circulation Ψ_{eq} (the vertically averaged overturning streamfunction at the equator) and the density difference, $\rho_N - \rho_S$, between the north pole and south pole. (b) The proportional relationship between the meridional heat transport across the equator \mathcal{H}_{eq} and the product of $\Psi_{eq} \Delta_z T$, where Ψ_{eq} is the cross-equatorial mass exchange, and $\Delta_z T$ is the top-minus-bottom temperature difference at the equator, which is typically negative. Dots in (c) show the cross-equatorial heat transport \mathcal{H}_{eq} as a function of core/shell heat partition. In all panels, each dot represents one experiment with a specific ice-core heat partition (denoted by the color of the dot) and ocean salinity (denoted by the size of the dot). The grey shading in panel (c) delineates the possible ranges of cross-equatorial heat transport if only the bottom heating was redistributed. Dashed curves shown in panel (c) are the equilibrium \mathcal{H}_{eq} for two groups of experiments initialized from different initial conditions. Red curves show the equilibrium \mathcal{H}_{eq} against the core/shell heat partition for experiments initialized by the equilibrium fluid state of the experiment with 100% core-heating. Blue curves show the same but for experiments initialized using experiment with 80% heat generated in the ice shell.

184 be measured by the vertically averaged mass-transport streamfunction at the equator, Ψ_{eq} , and by the top-minus-bottom
 185 temperature difference $\Delta_z T$. As can be seen in Fig.4b, the diagnosed cross-equatorial heat transport correlates very
 186 nicely with $C_p \Psi_{\text{eq}} \Delta_z T$ (here $C_p = 4000 \text{ J/kg/K}$ is the heat capacity of water). When heat production is predominantly
 187 in the core (denoted by reddish dots) equilibrium solutions are spread in the first quadrant of the diagram, which
 188 corresponds to energy gain in the northern hemisphere; when heat production is in the ice shell (bluish dots) solutions
 189 congregate in the third quadrant with southward heat transport at the equator. In all experiments, temperature increases
 190 with depth at the equator ($\Delta_z T < 0$): for those with core heating, the bottom water is naturally warmer; for those
 191 without, $|\Delta_z T|$ is much smaller but remains negative because the temperature at the equatorial water-ice interface is
 192 close to the local freezing point, which is strongly depressed due to the thick ice shell there. We see then that the
 193 direction of inter-hemispheric heat transport is controlled by the sign of Ψ_{eq} .

194 The cross-equatorial overturning, Ψ_{eq} , is driven by the density difference between the two hemispheres (Fig.3-c).
 195 The two correlate very well, as can be seen in the scatter plot in Fig.4a of Ψ_{eq} vs the pole-to-pole density difference
 196 $\rho_N - \rho_S$. This strong correlation is likely to stem from the positive feedback between the two variables: if water in
 197 the northern hemisphere is generally denser than in the southern hemisphere ($\rho_N - \rho_S > 0$), a positive Ψ_{eq} will be
 198 induced. Given that $\Delta_z T < 0$, ocean circulation will then transport heat into the southern hemisphere, facilitating
 199 melting there and further increasing the density contrast $\rho_N - \rho_S$. Ocean salinity affects the strength of this positive
 200 feedback, by regulating the amount of salinity change induced per unit amount of freezing/melting. This is why high
 201 salinity experiments (denoted by dots of larger size) are found farther away from the origin in Fig.4a. In the presence
 202 of a positive feedback, the cross-equatorial circulation and heat transport, once activated, will amplify over time until
 203 being stabilized — as Ψ_{eq} strengthens, salinity gradients induced by the ice freezing/melting will be smoothed out
 204 more readily, limiting the salinity gradient that can be sustained.

205 Constrained positive feedback is known to be the key to systems which exhibit hysteresis and bistable behavior
 206 (Meadows et al., 1997). To seek multiple equilibrium solutions for each parameter set, we ran the same experiments
 207 across our salinity and core/shell heat partitions, but instead of initializing the model with zero salinity variations
 208 and zero flow, we used the equilibrium fluid state (temperature, salinity and flow field) of experiments with 0% shell-
 209 heating, which exhibit strong northward heat transport across the equator and with 80% shell-heating, which exhibit
 210 strong southward heat transport. As shown by the dashed curves in Fig.4c, when initialized from the equilibrium state
 211 with 0% shell-heating (red dashed curves), more heat tends to be transported northward, in comparison to the same
 212 experiments initialized from the equilibrium state with just 80% shell-heating (blue dashed curves). Just as in a typical
 213 hysteresis diagram, the difference between the two sets of experiments maximizes when the heat partition is around
 214 50-50 and vanishes when the core-heat-partition or shell-heat-partition approaches 100%.

215 The direction of the cross-equatorial circulation, and thereby the ocean feedback onto ice shell hemispheric asym-

216 metry, is controlled by the initial pole-to-pole density difference, $\rho_N - \rho_S$, before any cross-equatorial circulation or
 217 heat transport has formed. If water in the northern hemisphere is slightly heavier, ocean circulation would transport
 218 heat to the southern hemisphere, enhancing the preexisting asymmetry; if the opposite is true, the asymmetry would
 219 be suppressed. In principle, the density can be affected by both salinity and temperature. However, salinity dominates
 220 over temperature except for the deep ocean in cases such as S5s0 (column-2 of Fig.3) — this corresponds to a fresh
 221 ocean with a significant amount of heating from the core; because of anomalous expansion, the ocean is much warmer
 222 at the bottom whilst remaining stable.

223 Since salinity is always the dominant factor in setting pole-to-pole density differences thanks to the positive feed-
 224 back, we must understand which of the poles freezes/melts relative to the other before cross-equatorial heat transport
 225 begins to develop. There are three mechanisms that affect this “initial” freezing/melting: 1) conductive heat loss,
 226 $\mathcal{H}_{\text{cond}}$, will be more efficient over the south pole due to the relatively thin ice there; 2) since the ice shell is thinner
 227 over the south pole, more tidal heating, \mathcal{H}_{ice} , is produced there as a result of the ice rheology feedback (Beuthe, 2019;
 228 Kang and Flierl, 2020), leading to melting; 3) the ice thickness gradient is stronger in the southern hemisphere, and so
 229 will induce more equator-to-pole mixing, more equatorward heat transport due to the ice-pump mechanism (Lewis and
 230 Perkin, 1986; Kang et al., 2021), and hence more freezing at the south pole. The first and the last processes suppress
 231 hemispheric symmetry-breaking, whereas the second mechanism enhances symmetry-breaking. Only when the ice
 232 shell produces most of the heat, does the second mechanism dominate resulting in enhanced melting over the south
 233 pole (or less freezing) than the north pole. As time progresses the cross-equatorial ocean circulation then enhances
 234 this initial tendency. In this way, we can rationalize the ocean feedback on core/shell heat partition shown in Fig.2a.

235 Whether melting of ice occurs more at the north pole vs the south pole depends on the sign of (see Eq.13):

$$L\Delta q = \Delta\mathcal{H}_{\text{cond}} - \Delta\mathcal{H}_{\text{ice}} - \Delta\mathcal{H}_{\text{ocn}}$$

236 where Δ denotes the difference between the quantity evaluated over the north pole and the south pole and q is the
 237 freezing rate. The difference between $\mathcal{H}_{\text{cond}}$ and \mathcal{H}_{ice} over the two poles can be quantified given that the ice over the
 238 south polar regions is about 30% thinner than that over the north pole ($\Delta H/H = 0.3$, see black solid curve in Fig. 1b).
 239 Since the conductive heat loss $\mathcal{H}_{\text{cond}}$ (Eq.8) is inversely proportional to the ice thickness H and the ice tidal dissipation
 240 \mathcal{H}_{ice} (Eq.10) is proportional to H raised to the power p_α (set to -2 in this study), the relative melt rate is:

$$\begin{aligned}
 L\Delta q &= -\mathcal{H}_{\text{cond}} \frac{\Delta H}{H} - p_\alpha \mathcal{H}_{\text{ice}} \frac{\Delta H}{H} - \Delta\mathcal{H}_{\text{ocn}} \\
 &= -\left[\mathcal{H}_{\text{cond}} + s p_\alpha \mathcal{H}_{\text{ice}}^{(s=100\%)}\right] \frac{\Delta H}{H} - \Delta\mathcal{H}_{\text{ocn}}, \quad (1)
 \end{aligned}$$

241 where s is the percentage of heat produced by the ice, the superscript ($s = 100\%$) denotes the 100% shell-heating
 242 scenario and \mathcal{H}_{ocn} denotes the heat flux transmitted from the ocean to the ice. As can be read off from Fig. 1b, $\mathcal{H}_{\text{ice}}^{s=100\%}$
 243 is roughly 1.5 – 2 times as large as $\mathcal{H}_{\text{cond}}$ in high latitudes. Therefore, more freezing occurs in the north relative to the
 244 south ($\Delta q > 0$) only if $s > 30\%$ with $p_\alpha = -2$, if we neglect $\Delta\mathcal{H}_{\text{ocn}}$. Since the ice pump mechanism will likely be
 245 stronger given the steeper ice topography in the south, $\Delta\mathcal{H}_{\text{ocn}}$ should make a positive contribution. This implies that
 246 the transition from asymmetry-suppressing to asymmetry-enhancing might occur at even higher s , aligned with our
 247 results (Fig.2a).

248 Typically, once cross-equatorial heat transport has commenced, it strengthens over time whilst remaining the same
 249 sign, until an equilibrium is achieved. The absolute value of \mathcal{H}_{eq} increases as more heat is generated in the core (Fig.4c).
 250 This is because $\Delta_z T$ becomes more negative because the ocean bottom is heated more in the presence of a stronger
 251 bottom heat flux. A consequence is that the strongest enhancement of asymmetry does not occur when heating is all
 252 produced in the shell. Instead, it occurs when the core makes a minor but non-negligible contribution to the total heat
 253 budget. As a by-product of the aforementioned positive feedback, in most cases the amplitude of \mathcal{H}_{eq} exceeds the total
 254 hemispheric core heat production (grey shading in Fig.4c), especially when there is significant core heat production.
 255 Therefore, although bottom heating makes $\Delta_z T$ more negative and affects $|\mathcal{H}_{\text{eq}}|$, it is the ocean-ice heat exchange that
 256 predominantly supports and balances the meridional heat transport.

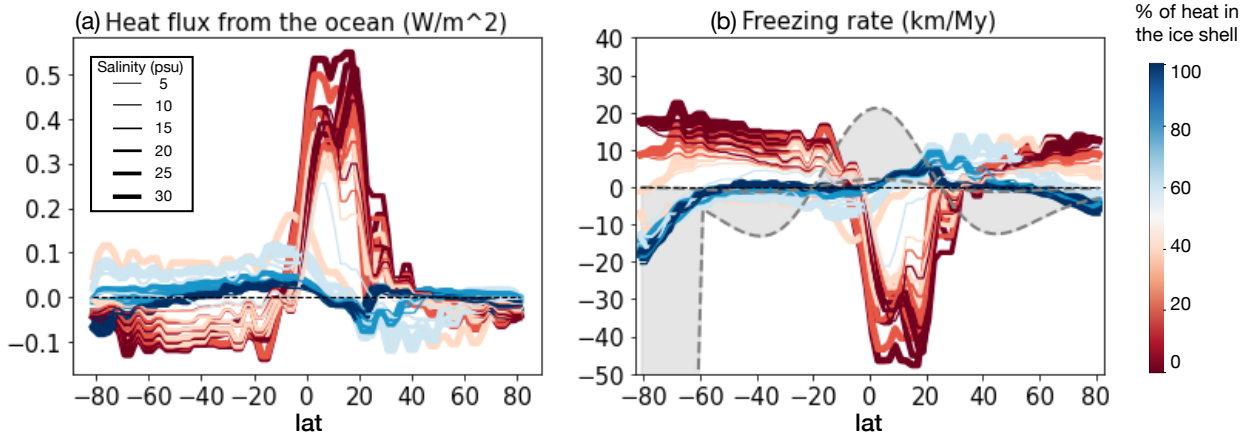


Figure 5: The ocean-ice heat exchange (left) and freezing rates (right) as a function of salinity (denoted by the line thickness) and core-shell heat partitions (denoted by the line color). The freezing/melting pattern required to balance the ice flow given the prescribed ice geometry is shown by two gray dashed curves, assuming two different ice viscosities ($\eta_{\text{melt}} = 10^{13}, 10^{14}$ Pa·s). Details of the ice flow model is given in appendix B. Since geysers over the south pole can remove significant amount of energy, and this process is not accounted for here, we set the “lower bound” of the freezing rate (corresponding to $\eta_{\text{melt}} = 10^{13}$ Pa·s) to negative infinity to the south of 60S. The gray shaded area in between is a measure of uncertainty.

257 Knowing the ocean-ice heat exchange (Fig. 5a), tidal dissipation in the ice and the conductive heat loss, we can
 258 estimate the freezing/melting pattern for each scenario (Fig. 5b). This allows us to infer ice shell evolution by comparing

259 this freezing rate with the thickness tendencies associated with the ice flow (the likely range is shown by the gray
 260 shading in Fig. 5), which transports ice from thick ice regions to thin ice regions under the influence of pressure
 261 gradient force (details of the ice flow model are given in appendix B). If the freezing rate is above the shaded zone, ice
 262 will grow and vice versa. In the shell-heating scenarios (shown by blueish curves), the hemispheric asymmetry will
 263 be enhanced. That said, the ocean heat transport mostly affects the low latitudes and mid-latitudes, inducing freezing
 264 around 20-60N and melting around 20S-20N. However, over geological timescales, the resultant thickness anomalies
 265 may be spread to the poles by ice flow. In contrast, the core-heating scenarios induce asymmetry which declines over
 266 time, due in part to the already weak ice-rheology feedback but also due to strong northward ocean heat transport.
 267 Moreover, because of the strong equatorward heat convergence in the core-heating scenarios ², the equatorial (polar)
 268 ice shell will inevitably thin (thicken) over time, aided by poleward ice flow directed down the thickness gradient. This,
 269 together with the asymmetry suppression observed in the core-heating scenarios, suggests to us that the source of heat
 270 on Enceladus comes predominantly from its ice shell rather than core. Hydrothermal activity at the sea floor may, of
 271 course, be an important local energy source for circulation (and life) but, just as on earth, it may not account for a large
 272 portion of the total heat source on Enceladus.

273 5. Summary of mechanisms and conclusions

274 We have found that heat transport by ocean circulation enhances hemispheric symmetry-breaking in ice thickness
 275 when heating primarily occurs in the ice shell driven by ocean tides, whilst if heating is primarily from the core, the
 276 ocean circulation acts as a damping of ice thickness asymmetry.

277 The mechanisms leading to cross-equatorial heat transport are sketched in Fig. 6. In the shell-heating scenario,
 278 heating concentrates at the south pole (shown by red shading) because the ice shell is thinner and hence more mobile
 279 there (Beuthe, 2019; Kang and Flierl, 2020). The conductive heat loss is also more efficient over the south pole (the
 280 red curly arrows atop of the ice shell) but is overwhelmed by tide-induced local heating. As a result, the south pole
 281 melts relative to the north. Over time, northern hemisphere waters becomes saltier and denser than in the southern
 282 hemisphere, driving an ocean circulation that sinks in the north and rises in the south (arrows). Since waters underneath
 283 the thick equatorial ice shell are the coldest of the global ocean, due to freezing point depression, such a circulation
 284 transports heat into the southern hemisphere, further thinning the ice shell there. The ocean circulation, therefore,
 285 results in patterns of melting and freezing which enhances inter-hemispheric gradients in ice thickness. This is balanced
 286 by transport of ice directed down the thickness gradient within the ice shell.

287 If, instead, the silicate core were to be the dominant heat source (see Fig. 6b), the ocean's overturning circulation

²Equatorward heat convergence melts the equatorial ice shell, reducing the local salinity and hence density, which in turn facilitates upward motions in the low latitudes. This will further enhance the equatorward heat convergence by bringing the bottom hot water toward equatorial ice shell. This cannot happen in experiments with prescribed freezing/melting rate as in Kang et al. (2021).

288 would reverse sign (arrows). This is because, even though core heat production remains symmetric between the two
 289 hemispheres, the south pole freezes more rapidly relative to the north due to the more efficient conductive heat loss
 290 there (red curly arrows at the top). With sinking now in the southern hemisphere and upwelling in the north, heat is
 291 transported northward across the equator reducing ice thickness in the north. The heat flux in the core heating case is
 292 typically much stronger than with shell-heating because the vertical temperature gradient at the equator is enhanced
 293 due to bottom heating. The ocean circulation, therefore, results in patterns of melting and freezing which reduce inter-
 294 hemispheric gradients in ice thickness. Since ice thickness gradients in the ice are also flattened by ice flow, it must be
 295 concluded that the end result is one in which ice thickness gradients have been smoothed out, at which point the ocean
 296 circulation and ice distributions would be symmetrically-disposed about the equator.

297 The above scenarios are not strongly affected by the ocean salinity, except that a salty ocean tends to facilitate a
 298 stronger positive feedback between the ice freezing/melting and the ocean circulation and thereby faster adjustment of
 299 ice shell geometry (see Fig.5).

300 Our results suggest, then, that the observed highly asymmetric Enceladean ice shell geometry (Iess et al., 2014;
 301 Tajeddine et al., 2017; Čadek et al., 2019; Hemingway and Mittal, 2019) is consistent with the primary energy source
 302 for ocean circulation being in the ice shell rather than the core. Such high dissipation rates in the ice shell may
 303 potentially be achieved through multiple scenarios as suggested by Tyler (2009, 2011, 2014, 2020), although current
 304 tidal models have difficulty achieving the high ice dissipation rate assumed here (Robuchon et al., 2010; Shoji et al.,
 305 2013; Běhounková et al., 2013; McCarthy and Cooper, 2016; Beuthe, 2019; Soucek et al., 2019; Gevorgyan et al.,
 306 2020).

307 For icy moons of size greater than Enceladus, most notably Europa, we expect the ocean circulation and heat
 308 transport to increase as gravity and hence surface forcing become stronger. This is because the pressure gradient at the
 309 ocean-ice interface will increase with gravity, and so give rise to greater shifts of freezing point, stronger temperature
 310 gradients and hence drive stronger ocean circulations. As a result, the role of ocean circulation may be to flatten
 311 out any equator-to-pole ice shell gradients on icy moons of larger size. Moreover, asymmetry may also be suppressed
 312 because of more efficient equator-to-pole heat transport (i.e., greater H_{ocn} in Eq.1) and a weakening of the ice-rheology
 313 feedback (smaller $H_{\text{ice}}/H_{\text{cond}}$ in Eq.1).

314 Finally, we should remind ourselves of the many caveats that accompany our study. First and foremost, to enable
 315 us to integrate our model long enough to reach equilibrium (many thousands of years), we use a zonally symmetric
 316 configuration in which transport by baroclinic eddies is missing. We note that meridional potential vorticity gradients
 317 change sign over the water column of our solutions (not shown), and so, by the Charney-Stern criterion (Charney and
 318 Stern, 1962), we might expect baroclinic instability to occur. These can facilitate jet formation and affect heat and
 319 tracer transport (Schneider, 2006). Their impact on cross-equatorial heat transport and the general circulation of icy

320 moons is an important topic for future study. Moreover, convection is parameterized in our model rather than resolved,
 321 and the bottom heating is assumed to be uniformly distributed, albeit slightly poleward-amplified (red dashed curve in
 322 Fig.1b). Convective plumes may significantly affect heat transport, especially if the heat flux becomes geographically
 323 localised and more intense, as suggested by Choblet et al. (2017). We also leave such issues for future study.

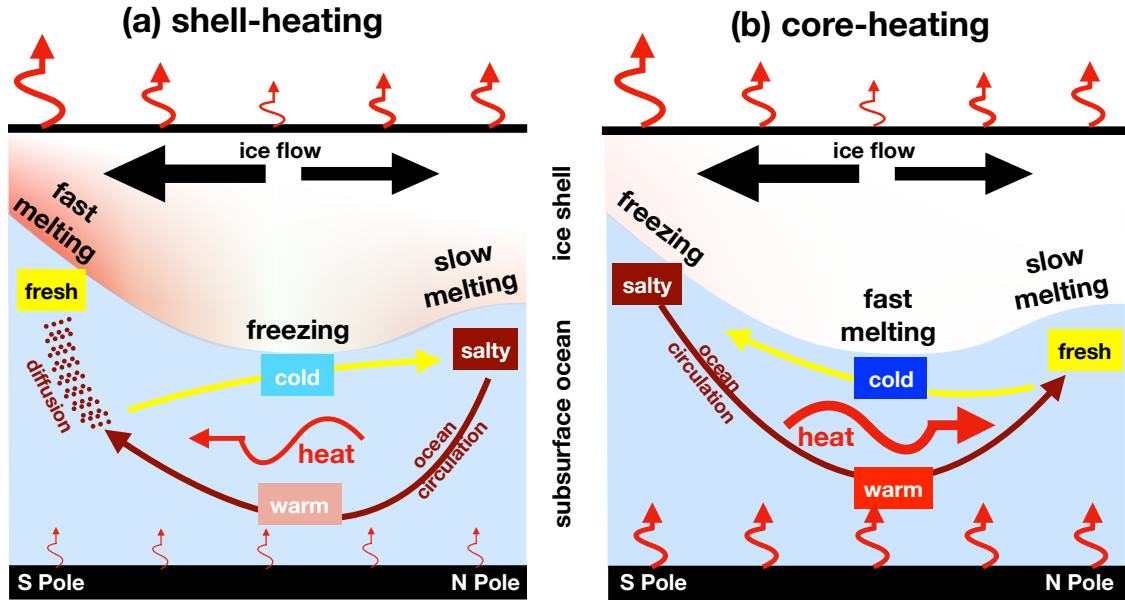


Figure 6: Schematics of ocean circulation and heat transport for the (a) shell-heating and (b) core-heating scenarios. Note that only the hemispherically-asymmetric patterns are shown. The upward-pointing curly red arrows show heat fluxes entering from the bottom and exiting at the top. The horizontally-directed curly red arrow shows the lateral heat transport by ocean circulation. The red shading in the ice shell mark the patterns of tidal heating which peak over the poles where the ice is thin, largest over the south pole. Broad patterns of melting and freezing are marked, together with the rate, along with the associated salinity anomalies. Melting and freezing are balanced by lateral ice transport within the ice shell, directed from thick to thin. Rates of melting (fast, slow) are based on consideration of Fig. 5b. The broad patterns of anomalous overturning circulation in the ocean are indicated by the thick curved arrows, which are color-coded to indicate the salt transport. Dark brown denotes the flow of dense salty water, light yellow that of buoyant fresh water. The water is coldest just under the thickest ice, which occurs at the equator. The water beneath is warmer, in part due to bottom heating. Water properties in different parts of the ocean are indicated by text boxes. See the main text for details.

324 Acknowledgments

325 This work was carried out in the Department of Earth, Atmospheric and Planetary Science (EAPS) in MIT. WK
 326 acknowledges support as a Lorenz/Houghton Fellow supported by endowed funds in EAPS. JM and SB acknowledge
 327 part-support from NASA Astrobiology Grant 80NSSC19K1427 “Exploring Ocean Worlds”. The supporting
 328 information provides detailed description of our model setup. Code and data is available upon reasonable request.

329 **A. Description of Ocean General Circulation Model**

330 To explore whether ocean circulation enhances or suppresses hemispheric asymmetries in the thickness of the ice
 331 shell of Enceladus, we model the large-scale overturning circulation in the Enceladean ocean encased by a hemispherically-
 332 asymmetric ice shell, and diagnose the resulting cross-equatorial heat transport. Given our uncertain knowledge of
 333 the mean salinity of the ocean and the partitioning of heat production in the core and the shell, we explore many (in
 334 fact 30) plausible combinations. The simulations are carried out using the state-of-the-art Massachusetts Institute of
 335 Technology ocean circulation model (MITgcm, MITgcm-group, 2010; Marshall et al., 1997) in a two-dimensional
 336 configuration (latitude and depth). The efficiency of the 2D setup enables us to integrate out the simulations to full
 337 equilibrium and explore a wide parameter space. Unless otherwise stated, initial current and salinity variations are set
 338 to zero and the initial potential temperature at each latitude set equal to the freezing point at the water-ice interface.
 339 From this initial state, each simulation is launched for 75,000 years, by which time equilibrium is reached.

340 The model integrates the non-hydrostatic primitive equations governing the motion of a fluid in height coordinates
 341 including a full treatment of all components of the Coriolis force. These components are typically ignored when
 342 simulating Earth’s ocean because of its small aspect ratio (the ratio between depth and horizontal scale of the ocean
 343 basin), but is crucial for Enceladus’s ocean, whose aspect ratio is instead order $40\text{km}/252\text{km} \sim 0.16$ and so not small.
 344 The size of each grid cell shrinks with depth due to spherical geometry and is accounted for by switching on the
 345 “deepAtmosphere” option of MITgcm. Since the depth of Enceladus’s ocean is comparable to its radius, the variation
 346 of gravity with depth is significant. The vertical profile of gravity in the ocean and ice shell is given by, assuming a
 347 bulk density of $\rho_{\text{out}} = 1000 \text{ kg/m}^3$:

$$g(z) = \frac{G [M - (4\pi/3)\rho_{\text{out}}(a^3 - (a - z)^3)]}{(a - z)^2}. \quad (2)$$

348 In the above equation, $G = 6.67 \times 10^{-11} \text{ N/m}^2/\text{kg}^2$ is the gravitational constant and $M = 1.08 \times 10^{20} \text{ kg}$ and $a = 252 \text{ km}$
 349 are the mass and radius of Enceladus.

350 Since it takes many tens of thousands of years for our solutions to reach equilibrium, we employ a moderate
 351 resolution of 2 degree (8.7 km) and run in a 2D, zonal-average configuration whilst retaining full treatment of Coriolis
 352 terms. By so doing, zonal variations are omitted. In the vertical direction, the 60 km ocean-ice layer is separated into
 353 30 layers, each of which is 2 km deep. The ocean is encased by an ice shell with meridionally-varying thickness using
 354 MITgcm’s “shelfice” and ice “boundary layer” module (Losch, 2008). We employ partial cells to better represent the
 355 ice topography: water is allowed to occupy a fraction of the height of a whole cell with an increment of 10%.

356 We set the ice thickness H to be slightly asymmetric between the two hemispheres and thin towards each pole:

$$H(\phi) = H_0 + H_2 P_2(\phi) + H_1 P_1(\phi), \quad (3)$$

357 where $H_0 = 20.8$ km is the mean ice thickness. The constants $H_2 = -12.1$ km and $H_1 = 2$ km set the equator-to-pole
 358 and pole-to-pole thickness variations, respectively and P_1 , P_2 are the first and second Legendre Polynomials. The
 359 thickness variation is plotted in the thick black solid curve in Fig. 1b.

360 We explore a wide range of background salinities from 4 psu to 40 psu, and adopt a linear equation of state (EOS,
 361 which determines how density depends on temperature, salinity and pressure) to make the dynamics as transparent as
 362 possible. The dependence of potential density ρ on potential temperature θ and salinity S is set equal to:

$$\rho(\theta, S) = \rho_0 [1 - \alpha_T(\theta - \theta_0) + \beta_S(S - S_0)] \quad (4)$$

$$\rho_0 = \rho(\theta_0, S_0). \quad (5)$$

363 Here, ρ_0 , θ_0 and S_0 are the reference potential density, potential temperature and salinity, and α_T and β_S are the thermal
 364 expansion and haline contraction coefficients respectively, given by the first derivative of the density with respect to
 365 potential temperature and salinity at the reference point, obtained using the Gibbs Seawater Toolbox (McDougall and
 366 Barker, 2011). We carried out two test experiments (one with $S_0 = 10$ psu and the other with $S_0 = 20$ psu) using the
 367 full ‘‘MDJWF’’ equation of state (McDougall et al., 2003) and obtained almost identical results.

368 S_0 is prescribed a constant value between 5 psu and 30 psu. θ_0 is set to be the freezing temperature at S_0 and
 369 $P_0 = 2.2 \times 10^6$ Pa (this is the pressure under a 20.8 km thick ice sheet on Enceladus). Generally, the freezing point T_f
 370 depends on local pressure P and salinity S following

$$T_f(S, P) = c_0 + b_0 P + a_0 S, \quad (6)$$

371 where the constants are ascribed the following values: $a_0 = -0.0575$ K/psu, $b_0 = -7.61 \times 10^{-4}$ K/dbar and $c_0 =$
 372 0.0901 degC. The pressure P can be calculated using hydrostatic balance: $P = \rho_i g H$ where $\rho_i = 917$ kg/m³ is the
 373 density of the ice and H its thickness).

374 A.1. Representation of subgrid-scale processes

375 To account for the mixing of momentum, heat and salinity by turbulence that is not resolved, we set the explicit
 376 viscosity/diffusivity to be much larger than molecular values. There is no attempt to represent baroclinic instability.
 377 The default horizontal and vertical diffusivity are set to 0.001 m²/s to represent the mixing induced by high-frequency

378 turbulence driven by tides and libration (Tyler, 2020). This is 3 orders of magnitude or so greater than the molecular
 379 diffusivity, but is consistent with the dissipation rate estimated by a recent study (Rekier et al., 2019), in which both
 380 libration and tidal forcing were accounted for. According to Rekier et al. (2019), the tidal dissipation in the ocean is
 381 mostly induced by librations with a global dissipation rate E of around 1 MW. Following the review of Wunsch and
 382 Ferrari (2004), the vertical diffusivity can be estimated as

$$\kappa_v = \frac{\Gamma \varepsilon}{\rho_0 N^2}, \quad (7)$$

383 where $\Gamma \sim 0.2$ is the efficiency by which kinetic energy dissipation can be used to produce potential energy, $\varepsilon = E/V$
 384 is the ocean dissipation rate per unit area, $V = 4\pi a^2 D$ is the total volume of the Enceladean ocean, $\rho_0 \sim 1000 \text{ kg/m}^3$
 385 is the density of water, $N^2 = g(\partial \ln \rho / \partial z) \sim g(\Delta \rho / \rho_0) / D$ is the Brunt-Vaisala frequency. Assuming that $\Delta \rho / \rho_0$ is
 386 just $\alpha_T \Delta T_f$, where ΔT_f is the equator-to-pole temperature contrast, setting $\alpha_T \sim 1 \times 10^{-5} / \text{K}$ and $\Delta T_f \sim 0.1 \text{ K}$, and
 387 substituting the above values into Eq.7, we find $\kappa_v \sim 0.001 \text{ m}^2/\text{s}$. This is the default horizontal and vertical diffusivity
 388 used in our model. The diffusivity for temperature and salinity are set to be the same, so that any double diffusive
 389 effects are suppressed.

390 Due to the relatively coarse model resolution, convective processes are not resolved. For regions that are convec-
 391 tively unstable, we overwrite the vertical diffusivity with a much greater value, $1 \text{ m}^2/\text{s}$, to represent the vertical mixing
 392 associated with small-scale convective motions. Such approaches are widely used to parameterize convection in coarse
 393 resolution ocean models. Results are not found to be sensitive to this choice as long as the associated diffusive time
 394 scale $D^2 / \nu_{\text{conv}} \approx 0.5 \text{ yr}$ is much shorter than the advective time scale $M_{\text{half}} / \Psi \approx 2000 \text{ yrs}$ (M_{half} is half of the total
 395 mass of the ocean and Ψ is the maximum meridional streamfunction in kg/s).

396 The horizontal and vertical viscosity are set to $1 \text{ m}^2/\text{s}$ to retain a smooth solution on the grid-scale and to make sure
 397 that the Ekman boundary layer is thick enough to be resolved. To damp grid-size noise induced by stair-like topography,
 398 we introduce a bi-harmonic hyperviscosity of $1 \times 10^8 \text{ m}^4/\text{s}$ and a bi-harmonic hyperdiffusivity of $1 \times 10^7 \text{ m}^4/\text{s}$ in addition
 399 to the harmonic mixing terms. Adding a scale-selective viscosity stabilizes the model and smooths the solution, whilst
 400 retaining large-scale features.

401 To demonstrate that the viscous terms indeed play a minor role, Fig. 7 shows, for one example case (S30s80),
 402 that the two terms in the thermal wind balance — $2\mathbf{\Omega} \cdot \nabla U = \partial b / \partial \theta$ — balance one-another. Since thermal wind
 403 is a consequence of geostrophic and hydrostatic balance, and on the large scale hydrostatic balance is always a good
 404 approximation, geostrophic balance must also be satisfied.

405 A.2. Heat budget

406 Heat is lost in our system through heat conduction across the ice shell, $\mathcal{H}_{\text{cond}}$, which can be estimated using a 1D
 407 vertical heat conduction model,

$$\mathcal{H}_{\text{cond}} = \frac{\kappa_0}{H} \ln \left(\frac{T_f}{T_s} \right), \quad (8)$$

408 given the thickness of the ice H (Hemingway and Mittal, 2019) (black solid curve in Fig. 1b), the surface T_s (set to the
 409 radiative equilibrium temperature of Enceladus assuming an albedo of 0.8) and an ice temperature near the water-ice
 410 interface, which, by definition, is the local freezing point T_f given by Eq. 6. This yields a heat loss rate of roughly
 411 50 mW/m², as shown by the green dashed curve in Fig. 1b of the main text).

412 This loss is counterbalanced by tidal heating in the ice shell, \mathcal{H}_{ice} , and the core, $\mathcal{H}_{\text{core}}$. Heating in the shell is
 413 forced by ocean tides³, but tidal dissipation within the ocean itself is likely to play only a secondary role due to the
 414 presence of the the ice shell (Chen, E M A and Nimmo, F, 2011; Beuthe, 2016; Hay and Matsuyama, 2019; Requier
 415 et al., 2019), except if the ocean is in a resonant state Tyler (2008, 2011, 2014). For each assumed heat partition, we
 416 use the same heating profiles for $\mathcal{H}_{\text{core}}$ and \mathcal{H}_{ice} (see below).

417 According to Beuthe (2019) and Choblet et al. (2017), the core dissipation $\mathcal{H}_{\text{core}}$ peaks at the two poles. We obtain
 418 the meridional heat profile using Eq.60 in Beuthe (2019) (Beuthe, 2020, private communication,

$$\mathcal{H}_{\text{core}}(\phi) = \mathcal{H}_{\text{core}}(\phi) = \overline{\mathcal{H}_{\text{core}}} \cdot (1.08449 + 0.252257 \cos(2\phi) + 0.00599489 \cos(4\phi)), \quad (9)$$

419 where ϕ is the latitude and $\overline{\mathcal{H}_{\text{core}}}$ is the global mean heat flux at the bottom. Since the global surface area shrinks going
 420 downward due to the spherical geometry, a factor of $(a - H)^2 / (a - H - D)^2$ (H is ice thickness, D is ocean depth)
 421 needs to be taken into account when computing $\overline{\mathcal{H}_{\text{core}}}$. The expression within the brackets above is normalized over
 422 the globe, and adjusted to take account of the fact that our model only covers 84S-84N. The above formula yields a
 423 bottom heat flux that is polar-amplified, as shown by the red dashed curve in Fig. 1b of the main text. This is prescribed
 424 as an upward geothermal heat flux from the lower boundary.

425 The remaining heat loss is balanced by tidal dissipation in the ice shell \mathcal{H}_{ice} . We calculate \mathcal{H}_{ice} using the thin ice
 426 shell model described in Beuthe (2019). Tidal dissipation consists of three components (Beuthe, 2019): a membrane
 427 mode $\mathcal{H}_{\text{ice}}^{\text{mem}}$ due to the extension/compression and tangential shearing of the ice membrane, a mixed mode $\mathcal{H}_{\text{ice}}^{\text{mix}}$ due
 428 to vertical shifting, and a bending mode $\mathcal{H}_{\text{ice}}^{\text{bend}}$ induced by the vertical variation of compression/stretching. Following
 429 Beuthe (2019), we first assume the ice sheet to be completely flat and solve for the dissipation rate $\mathcal{H}_{\text{ice}}^{\text{flat},x}$ (where
 430 $x = \{\text{mem}, \text{mix}, \text{bend}\}$). The ice properties are derived assuming a globally-uniform surface temperature of 60K and

³There have been some misunderstanding in the literature regarding whether crust (i.e., the ice shell) dissipation driven by ocean tide should be counted as ice dissipation or ocean dissipation. A detailed literature review and discussion is available in Tyler (2020).

431 a melting viscosity of 5×10^{13} Pa·s.

432 Ice thickness variations are accounted for by multiplying the membrane mode dissipation $\mathcal{H}_{\text{ice}}^{\text{flat,mem}}$, by a factor
 433 that depends on ice thickness. This makes sense because it is the only mode which is amplified in thin ice regions (see
 434 Beuthe, 2019). This results in the expression:

$$\mathcal{H}_{\text{ice}} = (H/H_0)^{p_\alpha} \mathcal{H}_{\text{ice}}^{\text{flat,mem}} + \mathcal{H}_{\text{ice}}^{\text{flat,mix}} + \mathcal{H}_{\text{ice}}^{\text{flat,bend}}, \quad (10)$$

435 where H is the prescribed thickness of the ice shell as a function of latitude and H_0 is the global mean of H . The tidal
 436 heating profiles are given as follows,

$$\mathcal{H}_{\text{ice}}^{\text{flat,mem}} = A (Y_{00} + 0.25Y_{20} + 0.0825Y_{40}) \quad (11)$$

$$\mathcal{H}_{\text{ice}}^{\text{flat,mem}} + \mathcal{H}_{\text{ice}}^{\text{flat,bend}} = A (0.124Y_{00} + 0.196Y_{20} - 0.0199Y_{40}), \quad (12)$$

437 where Y_{00} , Y_{20} , Y_{40} are spherical harmonics and A is a constant factor used to adjust the amplitude of \mathcal{H}_{ice} .

438 Since thin ice regions deform more easily and produce more heat, p_α is negative. Because more heat is produced
 439 in the ice shell, the overall ice temperature rises, which, in turn, further increases the mobility of the ice and leads to
 440 more heat production (the rheology feedback). We set $p_\alpha = -2$ here. \mathcal{H}_{ice} , rescaled to balance $\mathcal{H}_{\text{cond}}$, is shown by the
 441 blue solid curve in Fig. 1b. Those who are interested in further details of the model are encouraged to read Beuthe
 442 (2019).

443 A.3. Water-ice interaction

444 The interaction between the ocean and ice is simulated using MITgcm’s “shelf-ice” package (Losch, 2008; Holland
 445 and Jenkins, 1999). We turn on the “boundary layer” option to avoid possible numerical instabilities induced by an
 446 ocean layer which is too thin. The code is modified to account for a gravitational acceleration that is very different from
 447 that on earth, the temperature dependence of heat conductivity, and the meridional variation of tidal heating generated
 448 inside the ice shell and the ice surface temperature. Following Kang et al. (2020), the freezing/melting rate of the ice
 449 shell is determined by a heat budget for a thin layer of ice at the base⁴. The budget involves three terms: the heat
 450 transmitted from the ocean to the ice \mathcal{H}_{ocn} (positive upward), the heat loss through the ice shell due to heat conduction
 451 $\mathcal{H}_{\text{cond}}$ (Eq.8), and the tidal heating generated inside the ice shell \mathcal{H}_{ice} (Eq.10). As elucidated in Holland and Jenkins
 452 (1999) and Losch (2008), the continuity of heat flux and salt flux through the “boundary layer” gives,

$$\mathcal{H}_{\text{ocn}} - \mathcal{H}_{\text{cond}} + \mathcal{H}_{\text{ice}} = -L_f q - C_p(T_{\text{ocn-top}} - T_b)q \quad (13)$$

⁴This choice is supported by the fact that most tidal heating is generated close to the ocean-ice interface (Beuthe, 2018).

$$\mathcal{F}_{\text{ocn}} = -S_b q - (S_{\text{ocn-top}} - S_b)q, \quad (14)$$

453 where q denotes the freezing rate in $kg/m^2/s$, \mathcal{F}_{ocn} denotes the salinity flux (positive upward), $T_{\text{ocn-top}}$ and $S_{\text{ocn-top}}$
 454 is the temperature and salinity in the top grid of the ocean⁵, T_b and S_b denote the temperature and salinity in the
 455 imaginary “boundary layer”, where the water is just at the freezing point. $C_p = 4000$ J/kg/K is the heat capacity of the
 456 ocean, $L_f = 334000$ J/kg is the latent heat of fusion of ice. The last terms in Eq.13 and Eq.14 are associated with the
 457 warming/cooling and salinification/freshening required to convert ocean water to water in the “boundary layer”.

458 \mathcal{H}_{ocn} and \mathcal{F}_{ocn} in Eq.13 can be written as

$$\mathcal{H}_{\text{ocn}} = C_p(\rho_0\gamma_T - q)(T_{\text{ocn-top}} - T_b), \quad (15)$$

$$\mathcal{F}_{\text{ocn}} = (\rho_0\gamma_S - q)(S_{\text{ocn-top}} - S_b) \quad (16)$$

459 where $\gamma_T = \gamma_S = 10^{-5}$ m/s are the exchange coefficients for temperature and salinity, and T_b denotes the and tem-
 460 perature in the “boundary layer”. The terms associated with q are the heat/salinity change induced by the deviation
 461 of $T_{\text{ocn-top}}$, $S_{\text{ocn-top}}$ from that in the “boundary layer”, where melting and freezing occur. T_b equals the freezing
 462 temperature $T_f(S_b, P)$ (Eq.6) at pressure P and salinity S_b by definition. ρ_0 is the reference density (Eq.5).

463 The only two unknowns, S_b and q , in Eq. (13) and Eq. (14) can therefore be solved jointly. When freezing occurs
 464 ($q > 0$), salinity flux $\rho_{w0}\gamma_S(S_{\text{ocn-top}} - S_b)$ is negative (downward). This leads to a positive tendency of salinity at the
 465 top of the model ocean, together with changes of temperature.

$$\frac{dS_{\text{ocn-top}}}{dt} = \frac{-\mathcal{F}_{\text{ocn}}}{\rho_{w0}\delta z} = \frac{1}{\rho_{w0}\delta z}(\rho_{w0}\gamma_S - q)(S_b - S_{\text{ocn-top}}) = \frac{qS_{\text{ocn-top}}}{\rho_{w0}\delta z}, \quad (17)$$

$$\begin{aligned} \frac{dT_{\text{ocn-top}}}{dt} &= \frac{-\mathcal{H}_{\text{ocn}}}{C_p\rho_{w0}\delta z} = \frac{1}{\rho_{w0}\delta z}(\rho_{w0}\gamma_T - q)(T_b - T_{\text{ocn-top}}) \\ &= \frac{1}{C_p\rho_{w0}\delta z} [\mathcal{H}_{\text{ice}} - \mathcal{H}_{\text{cond}} + L_f q + C_p(T_{\text{ocn-top}} - T_b)q] \end{aligned} \quad (18)$$

466 where δz is the thickness of the upmost ocean grid.

467 The flow speed is relaxed to zero at the top boundary at a rate of $\gamma_M = 1 \times 10^{-3}$ m/s following

$$\frac{\partial u}{\partial t} = \dots - \frac{\gamma_M}{\delta z} u. \quad (19)$$

⁵When model resolution is smaller than the boundary layer thickness, the salinity below the upper-most grid cell also contributes to $T_{\text{ocn-top}}$ and $S_{\text{ocn-top}}$.

Symbol	Name	Definition/Value
a	radius of Enceladus	252 km
δ	obliquity of Enceladus	27°
A	albedo of Enceladus	0.81
H	global averaged ice shell thickness	20.8 km *
D	global averaged ocean depth	39.2 km *
Ω	rotation rate	$5.307 \times 10^{-5} \text{ s}^{-1}$
g_0	surface gravity	0.113 m/s^2
g	gravity in the ocean	Eq.2
L_f	latent heat of fusion of ice	334000 J/kg
C_p	heat capacity of water	4000 J/kg/K
$T_f(S, P)$	freezing point	Eq.6
ρ_i	density of ice	917 kg/m^3
ρ_w	density of the ocean	Eq.4
S_0	mean ocean salinity	5, 10, 15, 20, 25, 30 g/kg (psu)
P_0	reference pressure	$\rho_i g_0 H = 2.16 \times 10^6 \text{ Pa}$
T_0	reference temperature	$T_f(S_0, P_0)$
ρ_{w0}	reference density of ocean	Eq.5
α, β	thermal expansion & saline contraction coeff.	using Gibbs Seawater Toolbox **
κ_0	conductivity coeff. of ice	651 W/m^{***}
ν_h, ν_v	horizontal/vertical viscosity	$50 \text{ m}^2/\text{s}$
$\tilde{\nu}_h, \tilde{\nu}_v$	bi-harmonic hyperviscosity	$3 \times 10^9 \text{ m}^4/\text{s}$
κ_h, κ_v	horizontal/vertical diffusivity	$0.001 \text{ m}^2/\text{s}$
$(\gamma_T, \gamma_S, \gamma_M)$	water-ice exchange coeff. for T, S & momentum	$(10^{-5}, 10^{-5}, 10^{-3}) \text{ m/s}$
$\mathcal{H}_{\text{cond}}$	conductive heat loss through ice	Eq.8
\mathcal{H}_{ice}	tidal heating produced in the ice	Eq.10
$\mathcal{H}_{\text{core}}$	bottom heat flux powered by the core	Eq.9
ρ_a	ice dissipation amplification factor	-2

Table 1

Default model parameters. Ref *: Hemingway and Mittal (2019), ref **: McDougall and Barker (2011), ref ***: Petrenko and Whitworth (1999).

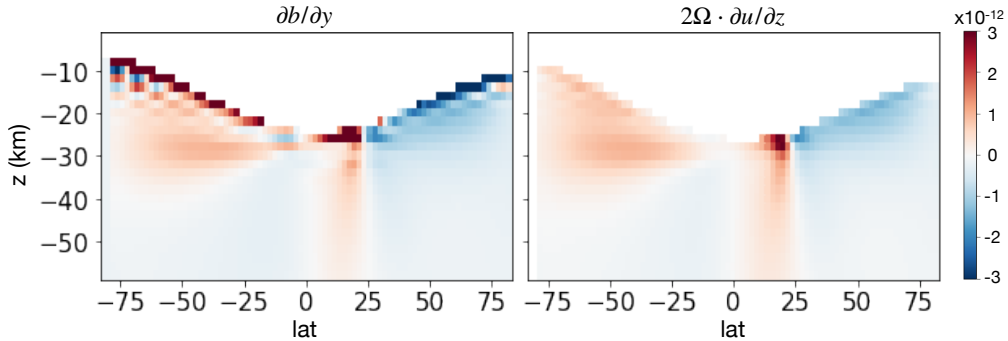


Figure 7: Balance of terms in the thermal wind balance. Left and right panels show the two terms in the thermal wind balance, $2\Omega \cdot \nabla U$ and $\partial b / \partial \theta$, respectively. Ω is the rotating angular speed, U is the zonal flow speed, $b = -g(\rho - \rho_0) / \rho_0$ is buoyancy, a is the moon's radius and θ denotes latitude. Away from the very near surface layers, there is very good balance.

468 B. Description of the ice flow model.

469 To compute the down-slope mass transport induced by ice thickness variation, we use an upside-down land ice
 470 sheet model following Ashkenazy et al. (2018). The ice flows down its thickness gradient, driven by the pressure

471 gradient induced by the spatial variation of the ice top surface, somewhat like a second order diffusive process. At
 472 the top, the speed of the ice flow is negligible because the upper part of the shell is so cold and hence rigid; at the
 473 bottom, the vertical shear of the ice flow speed vanishes, as required by the assumption of zero tangential stress there.
 474 This is the opposite to that assumed in the land ice sheet model. In rough outline, we calculate the ice flow using the
 475 expression below obtained through repeated vertical integration of the force balance equation (the primary balance
 476 is between the vertical flow shear and the pressure gradient force), using the aforementioned boundary conditions to
 477 arrive at the following formula for ice transport Q ,

$$\begin{aligned}
 Q(\phi) &= Q_0 H^3 (\partial_\phi H / a) & (20) \\
 Q_0 &= \frac{2(\rho_0 - \rho_i)g}{\eta_{\text{melt}}(\rho_0/\rho_i) \log^3(T_f/T_s)} \int_{T_s}^{T_f} \int_{T_s}^{T(z)} \exp\left[-\frac{E_a}{R_g T_f} \left(\frac{T_f}{T'} - 1\right)\right] \log(T') \frac{dT'}{T'} \frac{dT}{T}.
 \end{aligned}$$

478 Here, ϕ denotes latitude, $a = 252$ km and $g = 0.113$ m/s² are the radius and surface gravity of Enceladus, T_s and T_f are
 479 the temperature at the ice surface and the water-ice interface (equal to local freezing point, Eq. 6), and $\rho_i = 917$ kg/m³
 480 and ρ_0 are the ice density and the reference water density (Eq. 4). $E_a = 59.4$ kJ/mol is the activation energy for
 481 diffusion creep, $R_g = 8.31$ J/K/mol is the gas constant and η_{melt} is the ice viscosity at the freezing point. The latter
 482 has considerable uncertainty (10^{13} - 10^{16} Pa·s Tobie et al., 2003) but we choose to set $\eta_{\text{melt}} = 10^{14}$ Pa·s.

483 **References**

- 484 Ashkenazy, Y., Sayag, R., Tziperman, E., 2018. Dynamics of the global meridional ice flow of Europa's icy shell. *Nature Astronomy* 2, 43–49.
- 485 Baland, R.M., Yseboodt, M., Van Hoolst, T., 2016. The obliquity of Enceladus. *Icarus* 268, 12–31.
- 486 Běhouňková, M., Tobie, G., Choblet, G., Čadek, O., 2013. Impact of tidal heating on the onset of convection in Enceladus's ice shell. *Icarus*
487 226, 898–904.
- 488 Behouňkova, M., Tobie, G., Choblet, G., Čadek, O., 2012. Tidally-induced melting events as the origin of south-pole activity on Enceladus.
489 *Icarus* 219, 655–664.
- 490 Beuthe, M., 2013. Spatial patterns of tidal heating. *Icarus* 223, 308–329.
- 491 Beuthe, M., 2016. Crustal control of dissipative ocean tides in Enceladus and other icy moons. *Icarus* 280, 278–299.
- 492 Beuthe, M., 2018. Enceladus's crust as a non-uniform thin shell: I tidal deformations. *Icarus* 302, 145–174.
- 493 Beuthe, M., 2019. Enceladus's crust as a non-uniform thin shell: II tidal dissipation. *Icarus* 332, 66–91. doi:10.1016/j.icarus.2019.05.035.
- 494 Beuthe, M., Rivoldini, A., Trinh, A., 2016. Enceladus's and Dione's floating ice shells supported by minimum stress isostasy. *Geophysical Research*
495 *Letters* 43, 10,088–10,096.
- 496 Buckley, M.W., Marshall, J., 2016. Observations, inferences, and mechanisms of the atlantic meridional overturning circulation: A review. *Reviews*
497 *of Geophysics* 54, 5–63.
- 498 Čadek, O., Souček, O., Běhouňková, M., Choblet, G., Tobie, G., Hron, J., 2019. Long-term stability of enceladus's uneven ice shell. *Icarus* 319,
499 476–484.
- 500 Charney, J.G., Stern, M.E., 1962. On the stability of internal baroclinic jets in a rotating atmosphere. *Journal of Atmospheric Sciences* 19, 159–172.
- 501 Chen, E M A, Nimmo, F., 2011. Obliquity tides do not significantly heat Enceladus. *Icarus* 214, 779–781.
- 502 Choblet, G., Tobie, G., Sotin, C., Běhouňková, M., Čadek, O., Postberg, F., Souček, O., 2017. Powering prolonged hydrothermal activity inside
503 Enceladus. *Nature Astronomy* 1, 841–847.
- 504 Gevorgyan, Y., Boué, G., Ragazzo, C., Ruiz, L.S., Correia, A.C., 2020. Andrade rheology in time-domain. application to enceladus' dissipation of
505 energy due to forced libration. *Icarus* 343, 113610.
- 506 Glein, C., Postberg, F., Vance, S., 2018. The geochemistry of enceladus: Composition and controls. *Enceladus and the icy moons of Saturn* 39.
- 507 Han, L., Showman, A.P., 2010. Coupled convection and tidal dissipation in Europa's ice shell. *Icarus* 207, 834–844.
- 508 Hansen, C.J., Esposito, L., Stewart, A.I.F., Colwell, J., Hendrix, A., Pryor, W., Shemansky, D., West, R., 2006. Enceladus' Water Vapor Plume.
509 *Science* 311, 1422–1425.
- 510 Hay, H.C.F.C., Matsuyama, I., 2019. Nonlinear tidal dissipation in the subsurface oceans of Enceladus and other icy satellites. *Icarus* 319, 68–85.
- 511 Hemingway, D.J., Mittal, T., 2019. Enceladus's ice shell structure as a window on internal heat production. *Icarus* 332, 111–131.
- 512 Hemingway, D.J., Rudolph, M.L., Manga, M., 2019. Cascading parallel fractures on Enceladus. *Nature Astronomy* 311, 1–6.
- 513 Holland, D.M., Jenkins, A., 1999. Modeling Thermodynamic Ice–Ocean Interactions at the Base of an Ice Shelf. *J. Phys. Oceanogr.* 29, 1787–1800.
- 514 Howett, C.J.A., Spencer, J.R., Pearl, J., Segura, M., 2011. High heat flow from Enceladus' south polar region measured using 10-600 cm-1
515 Cassini/CIRS data. *Journal of Geophysical Research-Atmospheres* 116, 189.
- 516 Hsu, H.W., Postberg, F., Sekine, Y., Shibuya, T., Kempf, S., Horányi, M., Juhász, A., Altobelli, N., Suzuki, K., Masaki, Y., et al., 2015. Ongoing
517 hydrothermal activities within enceladus. *Nature* 519, 207–210.
- 518 Iess, L., Stevenson, D.J., Parisi, M., Hemingway, D., Jacobson, R.A., Lunine, J.I., Nimmo, F., Armstrong, J.W., Asmar, S.W., Ducci, M., Tortora,
519 P., 2014. The Gravity Field and Interior Structure of Enceladus. *Science* 344, 78–80.
- 520 Ingersoll, A.P., Nakajima, M., 2016. Controlled boiling on enceladus. 2. model of the liquid-filled cracks. *Icarus* 272, 319–326.

- 521 Kang, W., Bire, S., Campin, J.M., Sotin, C., German, C., Thurnherr, A., Marshall, J., 2020. Differing enceladean ocean circulation and ice shell
522 geometries driven by tidal heating in the ice versus the core. arXiv preprint arXiv:2008.03764 .
- 523 Kang, W., Flierl, G., 2020. Spontaneous formation of geysers at only one pole on enceladus's ice shell. PNAS 117, 14764–14768.
- 524 Kang, W., Mittal, T., Bire, S., Michel, J., Marshall, J., 2021. How does salinity shape ocean circulation and ice geometry on enceladus and other
525 icy satellites? arxiv .
- 526 Lewis, E., Perkin, R., 1986. Ice pumps and their rates. J. Geophys. Res 91, 756–11.
- 527 Losch, M., 2008. Modeling ice shelf cavities in a z coordinate ocean general circulation model. J. Geophys. Res. 113, 10.1029/2007JC004368.
- 528 Marshall, J., Adcroft, A., Hill, C., Perelman, L., Heisey, C., 1997. A finite-volume, incompressible Navier Stokes model for studies of the ocean on
529 parallel computers. J. Geophys. Res. 102, 5,753–5,766.
- 530 McCarthy, C., Cooper, R.F., 2016. Tidal dissipation in creeping ice and the thermal evolution of Europa. Earth and Planetary Science Letters 443,
531 185–194.
- 532 McDougall, T.J., Barker, P.M., 2011. Getting started with teos-10 and the gibbs seawater (gsw) oceanographic toolbox. SCOR/IAPSO WG 127,
533 1–28.
- 534 McDougall, T.J., Jackett, D.R., Wright, D.G., Feistel, R., 2003. Accurate and Computationally Efficient Algorithms for Potential Temperature and
535 Density of Seawater. Journal of Atmospheric and Oceanic Technology 20, 730–741.
- 536 Meadows, D., et al., 1997. Places to intervene in a system. Whole Earth 91, 78–84.
- 537 MITgcm-group, 2010. MITgcm User Manual. Online documentation. MIT/EAPS. Cambridge, MA 02139, USA.
538 http://mitgcm.org/public/r2_manual/latest/online_documents/manual.html.
- 539 Nimmo, F., Pappalardo, R.T., 2006. Diapir-induced reorientation of Saturn's moon Enceladus. Nature 441, 614–616.
- 540 Petrenko, V., Whitworth, R., 1999. Physics of Ice. OUP Oxford. URL: <https://books.google.com/books?id=oC941a81XWIC>.
- 541 Porco, C., Spitale, J., Mitchell, C., Dones, L., Ingersoll, A., West, R., 2007. Enceladus' jets: particle characteristics, surface source locations,
542 temporal variability, and correlations with thermal hot spots, in: Lunar and Planetary Science Conference, p. 2310.
- 543 Postberg, F., Kempf, S., Schmidt, J., Brilliantov, N., Beinsen, A., Abel, B., Buck, U., Srama, R., 2009. Sodium salts in e-ring ice grains from an
544 ocean below the surface of enceladus. Nature 459, 1098–1101.
- 545 Requier, J., Trinh, A., Triana, S., Dehant, V., 2019. Internal energy dissipation in enceladus's subsurface ocean from tides and libration and the role
546 of inertial waves. Journal of Geophysical Research: Planets 124, 2198–2212.
- 547 Roberts, J.H., Stickle, A.M., 2021. Breaking the symmetry by breaking the ice shell: An impact origin for the south polar terrain of enceladus.
548 Icarus , 114302.
- 549 Robuchon, G., Choblet, G., Tobie, G., Čadek, O., Sotin, C., Grasset, O., 2010. Coupling of thermal evolution and despinning of early iapetus. Icarus
550 207, 959–971.
- 551 Rozel, A., Besserer, J., Golabek, G J, Kaplan, M, Tackley, P J, 2014. Self-consistent generation of single-plume state for Enceladus using non-
552 Newtonian rheology. Journal of Geophysical Research: Planets 119, 416–439.
- 553 Schneider, T., 2006. The general circulation of the atmosphere. Annu. Rev. Earth Planet. Sci. 34, 655–688.
- 554 Shoji, D., Hussmann, H., Kurita, K., Sohl, F., 2013. Ice rheology and tidal heating of enceladus. Icarus 226, 10–19.
- 555 Soucek, O., Behoukova, M., Čadek, O., Hron, J., Tobie, G., Choblet, G., 2019. Tidal dissipation in Enceladus' uneven, fractured ice shell. Icarus
556 328, 218–231.
- 557 Spencer, J.R., Nimmo, F., 2013. Enceladus: An Active Ice World in the Saturn System. Annual Review of Earth and Planetary Sciences 41,
558 693–717.

- 559 Stegman, D.R., Freeman, J., May, D.A., 2009. Origin of ice diapirism, true polar wander, subsurface ocean, and tiger stripes of Enceladus driven
560 by compositional convection. *Icarus* 202, 669–680.
- 561 Tajeddine, R., Soderlund, K.M., Thomas, P.C., Helfenstein, P., Hedman, M.M., Burns, J.A., Schenk, P.M., 2017. True polar wander of Enceladus
562 from topographic data. *Icarus* 295, 46–60.
- 563 Thomas, P., Tajeddine, R., Tiscareno, M., Burns, J., Joseph, J., Loredo, T., Helfenstein, P., Porco, C., 2016. Enceladus's measured physical
564 libration requires a global subsurface ocean. *Icarus* 264, 37–47.
- 565 Tobie, G., Choblet, G., Sotin, C., 2003. Tidally heated convection: Constraints on Europa's ice shell thickness. *J. Geophys. Res - Atmospheres* 108,
566 219.
- 567 Tyler, R., 2011. Tidal dynamical considerations constrain the state of an ocean on Enceladus. *Icarus* 211, 770–779.
- 568 Tyler, R., 2014. Comparative estimates of the heat generated by ocean tides on icy satellites in the outer solar system. *Icarus* 243, 358–385.
- 569 Tyler, R.H., 2008. Strong ocean tidal flow and heating on moons of the outer planets. *Nature* 456, 770–772.
- 570 Tyler, R.H., 2009. Ocean tides heat enceladus. *Geophysical Research Letters* 36.
- 571 Tyler, R.H., 2020. Heating of enceladus due to the dissipation of ocean tides. *Icarus* 348, 113821.
- 572 Waite, J.H., Glein, C.R., Perryman, R.S., Teolis, B.D., Magee, B.A., Miller, G., Grimes, J., Perry, M.E., Miller, K.E., Bouquet, A., Lunine, J.I.,
573 Brockwell, T., Bolton, S.J., 2017. Cassini finds molecular hydrogen in the Enceladus plume: Evidence for hydrothermal processes. *Science* 356,
574 155–159.
- 575 Wunsch, C., 2005. Thermohaline loops, Stommel box models, and the Sandstrom theorem. *Tellus Series a-dynamic Meteorology and Oceanography*
576 57, 84–99.
- 577 Wunsch, C., Ferrari, R., 2004. Vertical mixing, energy and the general circulation of the oceans. *Ann. Rev. Fluid Mech.* 36, 281–314.
- 578 Young, W.R., 2010. Dynamic enthalpy, conservative temperature, and the seawater boussinesq approximation. *Journal of physical oceanography*
579 40, 394–400.
- 580 Zolotov, M.Y., 2007. An oceanic composition on early and today's Enceladus. *Geophysical Research Letters* 34.
- 581 Zolotov, M.Y., Postberg, F., 2014. Can nano-phase silica originate from chondritic fluids? The application to Enceladus' SiO₂ particles. *LPI* , 2496.